# Accepted Manuscript


Title: A combined phenomenological model for the representation of anisotropic hardening behavior in high strength steel line pipes

Authors: Y. Shinohara, Y. Madi, J. Besson

PII: S0997-7538(10)00082-3

DOI: 10.1016/j.euromechsol.2010.06.003

Reference: EJMSOL 2626

To appear in: *European Journal of Mechanics / A Solids*

Received Date: 21 April 2010

Revised Date: 21 June 2010

Accepted Date: 23 June 2010

Please cite this article as: Shinohara, Y., Madi, Y., Besson, J. A combined phenomenological model for the representation of anisotropic hardening behavior in high strength steel line pipes, European Journal of Mechanics / A Solids (2010), doi: 10.1016/j.euromechsol.2010.06.003

# A combined phenomenological model for the representation of anisotropic hardening behavior in high strength steel line pipes

Y. Shinohara[1], Y. Madi[1,2], J. Besson[1]

[1] *Centre des Matériaux, Mines ParisTech, UMR CNRS 7633 BP 87, 91003 Evry Cedex, France*

[2] *Ermess, EPF-Ecole d'Ingénieurs, Sceaux, France*

**Abstract**

Line pipes have anisotropic mechanical properties, such as tensile strength, ductility and toughness. These properties depend on both prestrain during the cold forming process and on the anisotropy of the mother plates. In this study, a phenomenological model combining isotropic and kinematic hardening is developed to represent anisotropic hardening behavior of high strength steel line pipes. The model is adjusted on experiments carried out on smooth and notched axisymmetric bars and plane strain specimens. The model is used to simulate bending tests carried out on large pipes containing a geometric imperfection. Numerical results suggest that prestraining in pipe forming process significantly affects the bending capacity of pipes.

*Key words:* Anisotropic plasticity. Kinematic hardening. Prestraining. Buckling. High strength steel. X100 steel.

## 1 Introduction

As consumption of energy is increasing worldwide, the demand for development of natural resources such as oil and gas in remote locations becomes strong. These development areas are often far from the major consumers because the potential locations are harsh environments where ground movement may occur due to loading by offshore ice, discontinuous permafrost or seismic activity. Ground movement will impose some strain demand on the pipelines (see e.g. (Lee et al., 2009)). For these reasons, strain-based design (SBD) is essential in the case of these types of harsh environments, while stress-based design of a pipeline is normally preferred. To achieve a safe and reliable pipeline operation in a harsh area, accurate prediction of the plastic strain imposed by the ground movement are required.

A pipe installed in such a field is subjected to plastic bending deformation. In SBD, the designers need to consider the imposed strain on both tensile and compressive sides of the bended pipe. Normally, full size pipe bending tests are carried out to evaluate the strain limit for buckling on compressive point, while curved wide plate tests are performed to predict the strain limit for ductile failure on the tension side (Fairchild et al., 2008). Numerical simulations by finite element analysis are also conducted for specifying the effective mechanical properties of the tested pipes and checking the predicted values against the experimental results (Tsuru et al., 2008).

The detailed mechanical properties of a line pipe have been clarified in the previous works (Shinohara et al., 2008; Tsuru et al., 2008). The line pipe has anisotropic hardening; a stress-strain curve is quite different between the longitudinal direction and the circumferential direction. These characteristics are mainly due to plastic strain developed during pipe forming. Furthermore, sharp texture of the mother plate, which is generated during thermomechanical control process (TMCP) at the plate mill, encourages anisotropy, especially in high strength line pipes (above X80 grade). Recently, it was pointed out that a buckling strain limit of the bended pipe is significantly affected by the anisotropic properties (Tsuru et al., 2008). It was also reported that anisotropic hardening has an influence on ductile crack driving force of a pipe pressured by the inner gas (Baek et al., 2010; Wang and Liu, 2007). However SBD of pipelines and in particular plastic instability of pipes have been investigated using rather simple models (i.e. von Mises or Hill plasticity with pure isotropic hardening) which could lead to poor predictions. Development of a model to represent anisotropic hardening and prestrain effect in a line pipe is therefore needed for SBD.

To simulate plastic behavior of the material after prestraining, it is necessary to combine isotropic and kinematic hardening together with plastic anisotropy. Several modeling strategies can be used. The first one, which will be used in this work, is based on phenomenological models which allow for a relatively simple identification of material parameters. As they use few material state variables, they can be used to perform large-scale computations. Mixed nonlinear isotropic and kinematic hardening can be represented following the approach proposed by Chaboche (1986). The model has been applied to aluminium alloys under cyclic loading (Hopperstad et al., 1995a,b). Other authors employed such a model to represent transient hardening of prestrained dual phase steels (Tarigopula et al., 2008, 2009). In these cases an isotropic stress measure was used to define the yield function. The von Mises stress measure is often used but the measure proposed in (Logan and Hosford, 1980) can also be used as in (Tarigopula et al., 2008). However, high strength pipeline steels have a strong anisotropic plasticity (Rivalin et al., 2000; Tanguy et al., 2008), so that an anisotropic yield function should be used. In (Chaboche, 2008) it was proposed to use the Hill quadratic function (Hill, 1950) together with mixed isotropic/kinematic hardening. However it is known that this function can hardly represent actual experimental data so that more complex yield function have been proposed in the literature (Barlat et al.,

1991; Bron and Besson, 2004; Karafillis and Boyce, 1993; Kim et al., 2007). However these complex yield surfaces have only been used assuming pure isotropic hardening. The second strategy is based on micromechanical polycrystalline models which use a physically based description of plastic slip in each grain and rules to describe the intergranular interaction (Hoc and Forest, 2001; Sai et al., 2006; Zouhal et al., 1996). Using the experimentally measured texture can help reducing the number of material parameters which need to be fitted. However parameters must be introduced to represent hardening of slip systems, interaction between slip systems and interaction between grains. In addition they use a large number of state variables thus significantly increasing the computation cost so that simulating structures becomes difficult. A third strategy is based on relatively simple macroscopic description but uses physically based state variables such as dislocation densities (see the original work by Mecking and kocks (1981)). Following this methodology, some authors (Haddadi et al., 2006) achieved accurate representations of the Bauschinger effect and transient hardening phenomena by prestraining, using a microstructural models proposed in (Teodosiu and Hu, 1995).

In this work, experiments are carried out on a API X100 grade line pipe steel plate in the as received state and for several levels of plastic prestrain. Experiments are carried out on smooth and notched axisymmetric bars and plane strain specimens along various loading directions to study both anisotropy and the effect of prestrain. A set of constitutive equations incorporating plastic anisotropy and mixed isotropic/kinematic hardening is proposed to represent the behavior of the material. The model is adjusted on the experimental data base and used to carry out simulation of large scale pipe bending experiments.

## 2 Material and experimental procedure

### *2.1 Material*

The material used in this study is a high-strength steel plate with 16mm thickness for line pipes produced in a commercial heavy plate mill. The chemical composition is shown in tab. 1. The plate was made through TMCP and accelerated cooling process in the mill. The microstructure is dual phase consisting of fine polygonal ferrite and bainite structure (see fig. 1).

The steel has anisotropic mechanical properties due to development of the crystallographic texture by TMCP, hence it is important to keep track of the material principal axes. In the following, the longitudinal direction, which is corresponding to the rolling direction, is referred to as L; the transverse direction is referred to as T and the short transverse (thickness) direction is referred to as S. D stands for the diagonal direction (45° between directions L and T in the sheet plane). The steel

| C | Si | Mn | P | S | Ti | N |
|---|---|---|---|---|---|---|
| 0.051 | 0.20 | 1.95 | 0.007 | 0.0015 | 0.012 | 0.004 |

Other alloying elements: Ni, Cr, Cu, Nb.

Table 1
Chemical composition of the used steel (weight %).

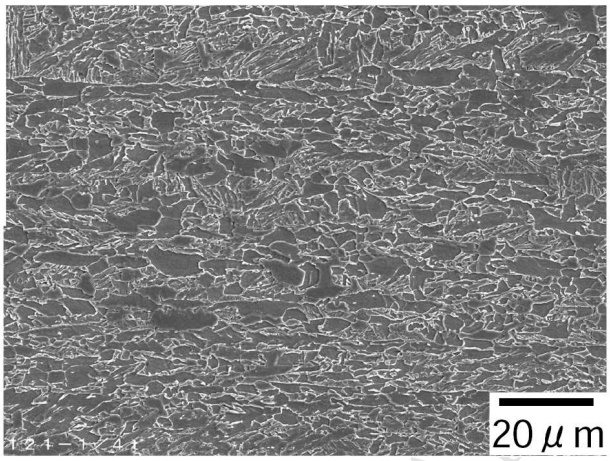


Fig. 1. SEM image of the steel plate used in this study (Nital etching).

strength after UOE forming [1] meets the API X100 grade specification where the yield strength is required 100 kpsi (or 690MPa) and higher.

### *2.2 Experimental procedure*

To obtain prestrained materials, prestrain tests were first conducted, using a 4000 kN tensile testing machine. Large flat tensile specimens (see fig. 2) were machined so that a 200mm$\times$100mm zone, where applied strain is uniform, could be produced at the center of the specimen. Strain gages were glued on the surface of tested specimens to check the actual prestrain level. The level of prestraining is up to 6.6%. Prestrain was performed along the T direction which corresponds to the main deformation direction during UOE forming.

A comprehensive characterisation of the mechanical properties of the steel was conducted along three different directions (L, T and D) using several types of tensile test specimens. The used geometries are presented in fig. 3. All tests were performed at room temperature on a servo-hydraulic testing machine for

[1] UOE forming is a manufacturing process where the plate material is first deformed into an U-shape then an O-shape. The pipe seam is then welded. The pipe is finally Expanded using an internal mandrel. To achieve low ovality, the pipe is typically expanded by 0.8–1.3% from its diameter after the O-step (Herynk et al., 2007).

the as-received and prestrained materials. Test specimens include smooth tensile bars (ST), axisymmetric notched bars with various notch radii ($\mathrm{NT}_\chi$) and plane strain specimens (PE). Notched bars, which are often used to characterize rupture (see e.g. (Mackenzie et al., 1977)), are employed here as they allow to induce stresses in directions perpendicular to the main loading direction (in particular along the S direction) and consequently allow to test multi-axial stress states using a simple experimental setup. In addition notched bars allow to reach high levels of deformation so that the hardening behaviour is determined over a wide range for plastic strain. This is an alternative to the sole use of tensile bars which then need to be analysed beyond necking to reach high deformation levels (Mirone, 2004; Zhang et al., 1999).

In the case of ST specimens, strain was measured using an extensometer with a gauge length equal to $L_0 = 9$ mm. $\Delta L$ denotes the gauge length variation. The imposed strain rate was: $\Delta\dot{L}/L_0 = 5.10^{-4}$ s$^{-1}$. In the case of ST and $\mathrm{NT}_\chi$ specimens the diameter reduction ($\Delta\Phi_\mathrm{S}$) in the minimum cross section was measured along the S direction along which deformation is maximum. For PE specimens, thickness reduction ($\Delta e$) was measured at the center of the specimen. For both $\mathrm{NT}_\chi$ and PE specimens the machine cross-head speed was selected so as to obtain a measured strain rate approximately equal to $5.10^{-4}$ s$^{-1}$. In the following $F$ denotes the force, $S_0$ the initial specimen minimum cross section, $\Phi_0$ the initial specimen minimum diameter and $e_0$ the initial PE specimen thickness.

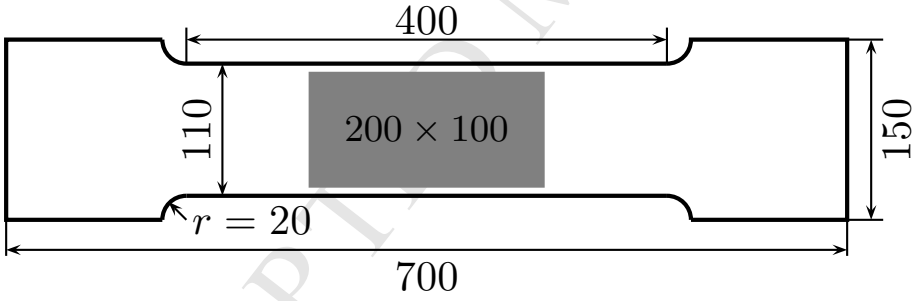


Fig. 2. Large tensile specimen for prestraining (dimension in mm). The gray area indicates the zone where prestrain is homogeneous.

## 3 Experimental results

### *3.1 Smooth tensile bars*

Fig. 4(a) shows nominal stress ($F/S_0$) vs nominal strain ($\Delta L/L_0$) curves in different loading directions of smooth tensile bar tests in the as received state. Flow stress depends on the loading direction. The flow stress in T load direction is the highest, while the one in D direction is the lowest. Plastic flow behavior

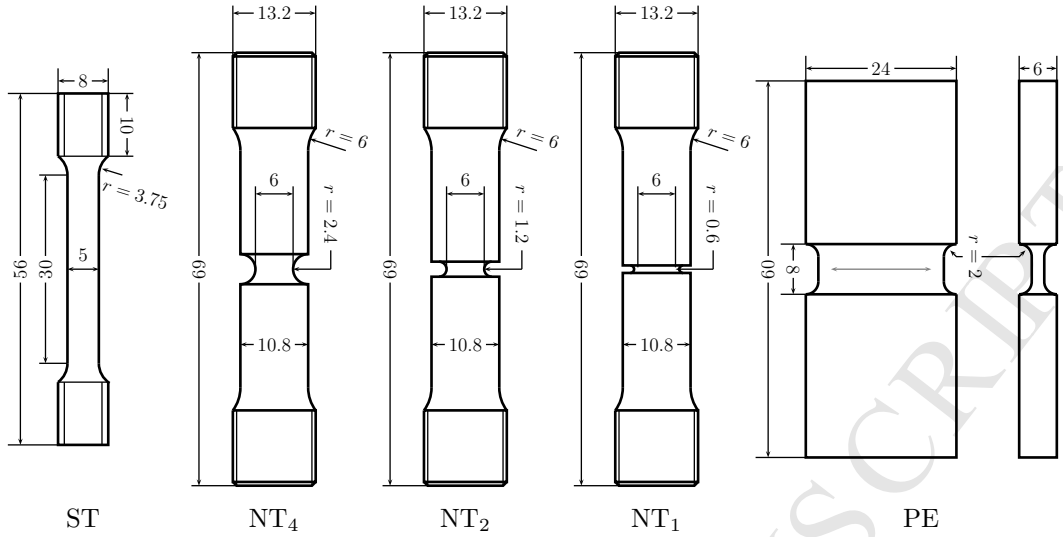


Fig. 3. Test specimens: ST: smooth tensile bar, $\mathrm{NT}_{\chi=1,\,2,\,4}$: axisymmetric notched bars, PE: plane strain specimens (the gray line indicates the plane strain direction).

also depends on the loading direction as shown in Fig. 4(b) where the diameter reduction $\Delta\Phi_S/\Phi_0$ is plotted as a function of the elongation $\Delta L/L_0$. In L and T loading, plastic anisotropy is obvious. Deformation along the S direction is larger than in the isotropic case so that initially round cross sections deform into ellipses (see e.g. (Tanguy et al., 2008)). On the other hand, D loading leads to an "isotropic" diameter reduction.

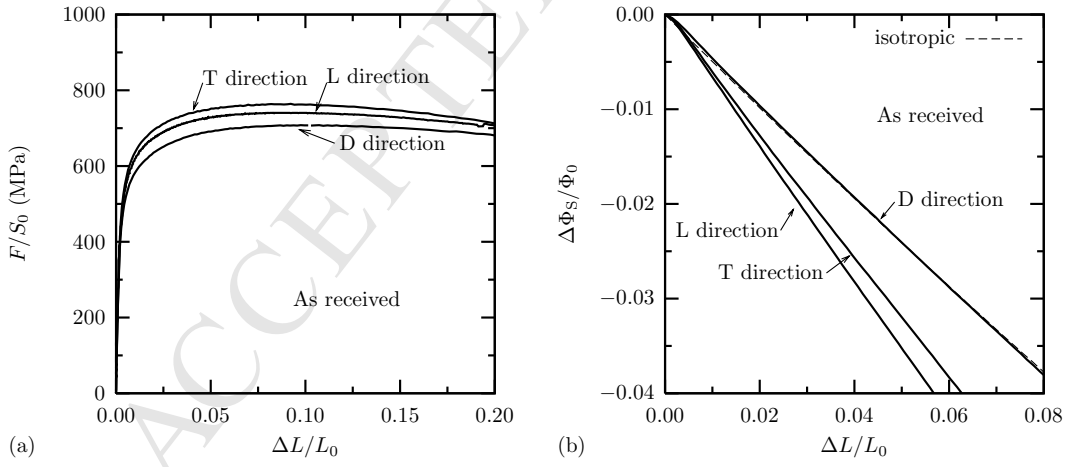


Fig. 4. (a) Nominal stress-strain curves in smooth bar tests of as-received steel. (b) Diameter reduction along the S direction as a function of elongation for L,T and D loading directions. The isotropic case corresponds to the equation: $\Delta\Phi_S/\Phi_0 = (1+\Delta L/L_0)^{-\frac{1}{2}} - 1$.

True stress-true strain curves of the smooth bar test for prestrained materials are shown in Fig. 5. True stress-true strain curves are computed assuming volume

conservation. The method is applied up to the ultimate tensile test (UTS). Stress-strain curves of the prestrained materials are shifted by the amount of prestrain. In T direction, which corresponds the prestraining direction, tensile tests on prestrained materials corresponds to elastic reloading up to the flow curve of the as-received material with a sharp transition between elastic and plastic regimes. Beyond yielding, curves coincide with that of the as-received material. On the other hand, in L direction (orthogonal one to the prestraining) and D direction (the 45° direction from T), the yield stress is higher than that of the as-received material but work hardening is rate continuously changing at the early strain stages with a smooth transition between elastic and plastic regimes. This behaviour is characteristic of mixed isotropic/kinematic hardening evidenced by performing strain-path changes (Tarigopula et al., 2009).

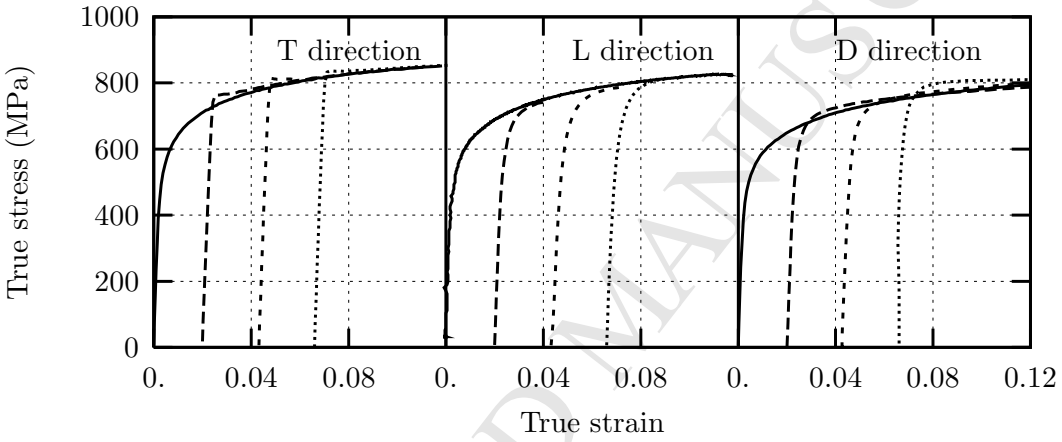


Fig. 5. True stress-strain curves in smooth bar tests of as-received and prestrain steels.

### *3.2 Notched bars*

Fig. 6 shows the normalized load ($F/S_0$) as a function of diameter reduction ($\Delta\Phi_S/\Phi_0$) for the various notched bars and for all prestrain levels. For a given testing condition (i.e. loading direction and prestrain level), maximum load increases with notch severity (Bridgman, 1952; Mackenzie et al., 1977) and ductility (characterized by the sharp load drop point) is reduced (Devillers-Guerville et al., 1997) as could be expected. A transient hardening (i.e. smooth transition between elastic and plastic regimes) behaviour is obtained for all cases. The transient hardening behaviour is still present for T loading on prestrained materials due to the development of a deformation gradient inside the notch (geometrical effect). With increasing prestrain level, maximum load increases and the radial strain at which the maximum load is reached decreases. For a given sample geometry and a given prestrain level, the maximum load is higher for T-loading due to both prestrain and the higher yield limit in the T-direction.

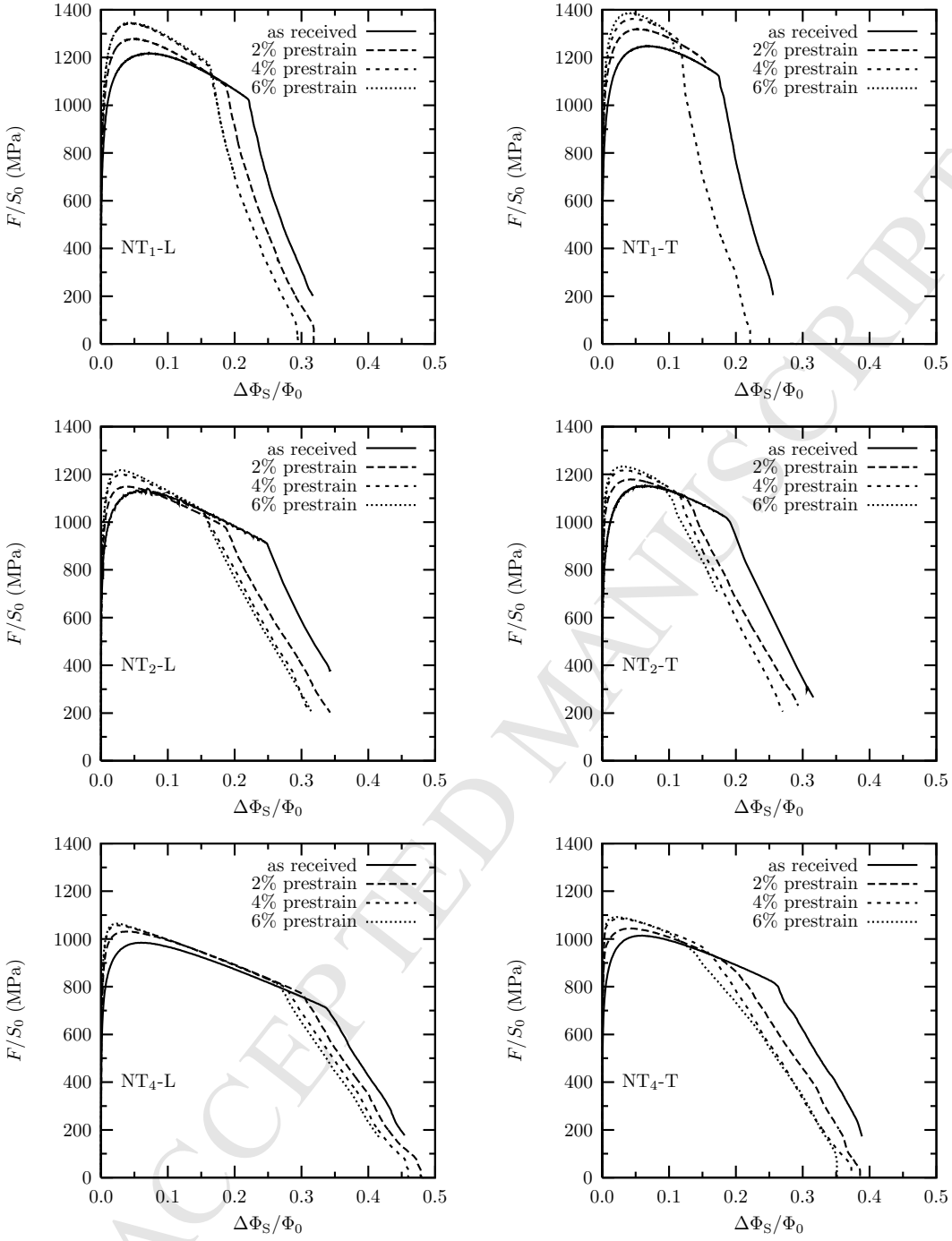


Fig. 6. Force-diameter reduction curves in notched bar tests of as-received and prestrained steels

### *3.3 Plane strain specimens*

Nominal stress-strain curves of plain strain tests for the as-received and 6% prestrained materials are shown in Fig. 7. In the as-received state, flow stress in

T load direction is larger than that in L. Especially, yield strength is much larger in T loading than in L. After 6% prestraining, work hardening is almost lost in both directions and the flow stress in T is still higher than in L.

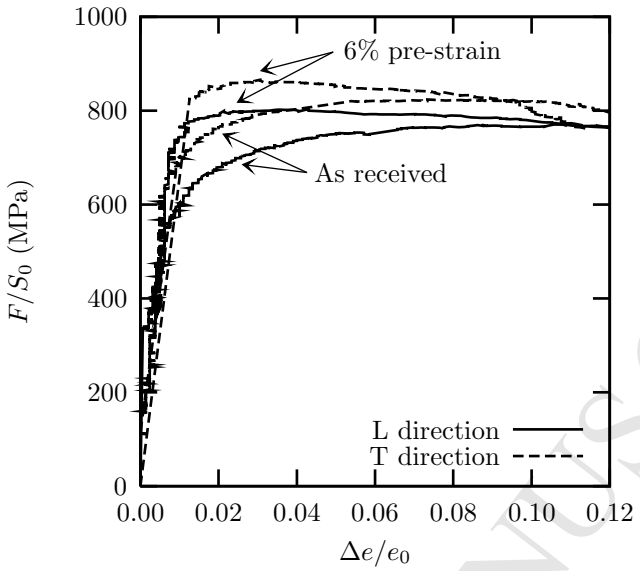


Fig. 7. Force-thickness reduction curves in plain strain tests of as-receive ed and prestrain steels

### *3.4 Strain rate sensitivity*

The material strain rate sensitivity was tested using three different strain rate : $5.10^{-5}$, $5.10^{-4}$ and $5.10^{-3}$ $s^{-1}$. Results are shown on fig. 8 for the as received material loaded along the L direction. A slight strain rate dependence is observed with stresses increasing with increasing strain rate.

## 4 Constitutive model

### *4.1 Constitutive equations*

The steel used in this study presents both anisotropic plasticity and kinematic hardening. The model proposed in the following accounts for both phenomena. In order to represent kinematic hardening, a back stress $\underline{X}$ is introduced (Chaboche, 1989). The yield surface is expressed using the difference ($\underline{B}$) between the Cauchy stress $\underline{\sigma}$ and the back stress: $\underline{B} = \underline{\sigma} - \underline{X}$. In order to account the anisotropic plasticity it is necessary to use an anisotropic stress measure to define the yield surface. The model proposed in (Bron and Besson, 2004) is used in the following. It consists in a generalization of of previously published models (Barlat et al.,

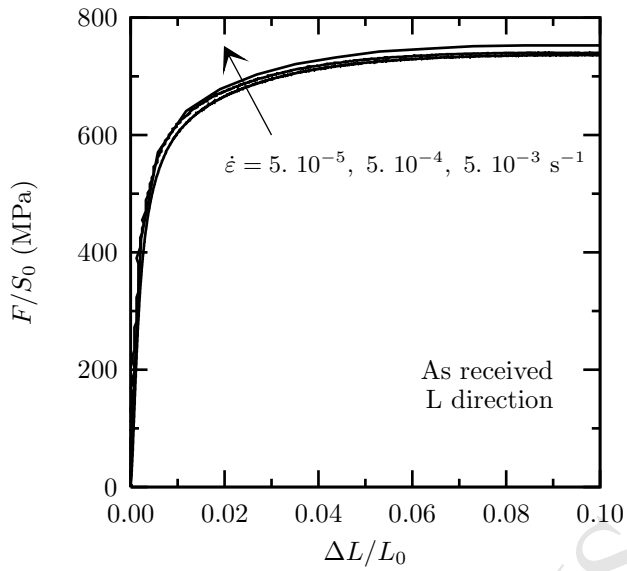


Fig. 8. Nominal stress-strain curves for various imposed strain rates (L direction, as-received steel).

1991; Karafillis and Boyce, 1993). For any symmetric second order tensor $\underline{T}$, the anisotropic scalar measure ($T_E$) is defined as:

$$\underline{T} \ \rightarrow \ T_E = \left( \sum_{k=1}^{N} \alpha_k T_{Ek}^a \right)^{1/a} \tag{1}$$

with $\sum_k \alpha_k = 1$ and $\alpha_k \geq 0, \forall k$. $a$ is a model coefficient. The function $T_E(\underline{T})$ is positive and homogeneous homogeneous of degree 1. $T_{Ek}$ are secondary anisotropic scalar measures. In the following, two measures will be used ($N = 2$) as in (Bron and Besson, 2004; Tanguy et al., 2008). One first defines two modified deviators:

$$\underline{T}_k = \underline{\underline{L}}_k : \underline{T} \qquad k = 1, 2 \tag{2}$$

where the fourth order tensor $\underline{\underline{L}}_k$ is expressed as using Voigt notations:

$$\underline{\underline{L}}_k = \begin{pmatrix} \frac{1}{3}(c^k_{\mathrm{LL}} + c^k_{\mathrm{SS}}) & -\frac{1}{3}c^k_{\mathrm{SS}} & -\frac{1}{3}c^k_{\mathrm{LL}} & 0 & 0 & 0 \\ -\frac{1}{3}c^k_{\mathrm{SS}} & \frac{1}{3}(c^k_{\mathrm{SS}} + c^k_{\mathrm{TT}}) & -\frac{1}{3}c^k_{\mathrm{TT}} & 0 & 0 & 0 \\ -\frac{1}{3}c^k_{\mathrm{LL}} & -\frac{1}{3}c^k_{\mathrm{TT}} & \frac{1}{3}(c^k_{\mathrm{TT}} + c^k_{\mathrm{LL}}) & 0 & 0 & 0 \\ 0 & 0 & 0 & c^k_{\mathrm{TL}} & 0 & 0 \\ 0 & 0 & 0 & 0 & c^k_{\mathrm{LS}} & 0 \\ 0 & 0 & 0 & 0 & 0 & c^k_{\mathrm{ST}} \end{pmatrix} \tag{3}$$

$c^{1,2}_{\mathrm{TT...ST}}$ are model coefficients. The eigenvalues of $\underline{T}_k$ are then computed: $T^1_k \geq T^2_k \geq T^3_k$. $T_{E1}$ is then computed as:

$$T_{E1} = \left(\frac{1}{2}\left(|T^2_1 - T^3_1|^{b_1} + |T^3_1 - T^1_1|^{b_1} + |T^1_1 - T^2_1|^{b_1}\right)\right)^{1/b_1} \tag{4}$$

and $T_{E2}$ as:

$$T_{E2} = \left(\frac{3^{b_2}}{2^{b_2}+2}\left(|T^1_2|^{b_2} + |T^2_2|^{b_2} + |T^3_2|^{b_2}\right)\right)^{1/b_2} \tag{5}$$

These definitions introduce two other model coefficients: $b_1$ and $b_2$.

The yield surface is then expressed using the above definition of the anisotropic stress measure as:

$$\phi = B_E - R(p) \tag{6}$$

where $R(p)$ represents isotropic hardening. Plastic flow is then computed using the normality rule as:

$$\underline{\dot{\varepsilon}}_p = \dot{p}\frac{\partial \phi}{\partial \underline{\sigma}} = \dot{p}\frac{\partial B_E}{\partial \underline{\sigma}} \tag{7}$$

where $\dot{p}$ is the plastic multiplier such that $\underline{\dot{\varepsilon}}_p : \underline{B} = \dot{p}B_E$. The evolution of the back stress is written using recall term to obtain non-linear (Armstrong–Frederick type) kinematic hardening (Chaboche, 2008):

$$\underline{\dot{X}} = \frac{2}{3}C\underline{\dot{\varepsilon}}_p - \dot{p}D\underline{X} \tag{8}$$

$C$ and $D$ are material parameters. In this study, only one back stress was used. The model can easily be extended to allow for a superposition of back-stresses (Chaboche, 2008; Samrout et al., 1997). To account for the slight strain rate dependence of the material, the plastic multiplier is expressed using Norton's law as:

$$\dot{p} = \dot{\varepsilon}_0(\phi/\sigma_0)^n \tag{9}$$

Finally a specific form for the $R$ function was chosen as:

$$R(p) = R_0\left(1 + Q_1(1 - \exp(-k_1 p)) + Q_2(1 - \exp(-k_2 p))\right) \tag{10}$$

### *4.2 Numerical analysis*

The proposed model in this study is implemented in the FE software Z-set (Besson and Foerch, 1997; Foerch et al., 1997). An implicit scheme is used to integrate the constitutive equations. The consistent tangent matrix is computed using the method proposed in (Simo and Taylor, 1985). Finite strains are accounted using a corotational frame as in (Sidoroff and Dogui, 2001).

| | |
|---|---|
| Elastic properties | |
| Young's modulus $E$ | 200 GPa |
| Poisson's ratio $\nu$ | 0.3 |
| Kinematic hardening | |
| $C$, $D$ | 39794 MPa, 287 |
| Isotropic hardening | |
| $R_0$ | 375.5 MPa |
| $Q_1$, $k_1$, $Q_2$, $k_2$ | 0.15, 78.6, 0.46, 18.8 |
| Strain rate dependence | |
| $\dot{\varepsilon}_0$, $\sigma_0$, $n$ | 1 $s^{-1}$, 55 MPa, 5 |
| Anisotropic yield model | |
| $a = b_1 = b_2$, $\alpha_1$, $\alpha_2$ | 8.74, 0.7, 0.3 |
| $c^1_{\mathrm{TT}}$, $c^1_{\mathrm{LL}}$ , $c^1_{\mathrm{SS}}$ | 1.05, 0.82, 0.66 |
| $c^1_{\mathrm{TL}}$, $c^1_{\mathrm{LS}}$ , $c^1_{\mathrm{TS}}$ | 0.93, 1.15, 1.19 |
| $c^2_{\mathrm{TT}}$, $c^2_{\mathrm{LL}}$ , $c^2_{\mathrm{SS}}$ | 0.94, 1.05, 0.74 |
| $c^2_{\mathrm{TL}}$, $c^2_{\mathrm{LS}}$ , $c^2_{\mathrm{TS}}$ | 0.80, 0.99, 1.17 |

Table 2
Material model parameters

### *4.3 Parameter identification*

The model developed in this study is complex and has several material parameters to be adjusted; the anisotropic yield function parameters ($a$, $b_1$, $b_2$, $\alpha$, $c^1_{\mathrm{TT...ST}}$, $c^2_{\mathrm{TT...ST}}$), the kinematic hardening parameters ($C$ and $D$) and the isotropic hardening parameters ($R_0$, $Q_1$, $Q_2$,$b_1$, $b_2$). In the following the model was simplified assuming $a = b_1 = b_2$. The parameter adjustment is carried out according to previous work (Bron and Besson, 2004). Tensile tests along L, T and D directions are used as well as all tests of notched bars with different minimum radii for the as-received and prestrained materials. In case of tensile smooth bars, force-axial displacement curves are used together with the relationship between axial and diameter displacement (fig. 4-b). In case of notched bars, force-diameter reduction curves are used. In both cases, diameter displacement is measured along S direction. Adjusted material model parameters are shown in tab. 2.

## 5 Numerical results and discussion

Fig. 9-(a)-(c) show the comparison of experimental and simulated true stress—true axial strain curves of smooth bar tests in different directions. For tests carried out on prestrained materials, the curves are shifted by the amount of plastic strain introduced by prestraining. As can be seen from these figures, the developed kinematic model can describe transient hardening at the early strain stage, which is dependent on reloading direction, after prestraining up to 0.06. For T loading direction, which is parallel to the prestrain direction, no transient stress-strain response is found, while in L and D directions, which are orthogonal and diagonal to the prestraining direction respectively, a significant change in stress-strain curve in the small strain region is indicated after the reloading.

Furthermore, as the developed model includes anisotropic yield function, it can represent anisotropic plastic flow for all loading directions as shown in Fig. 9-(d).

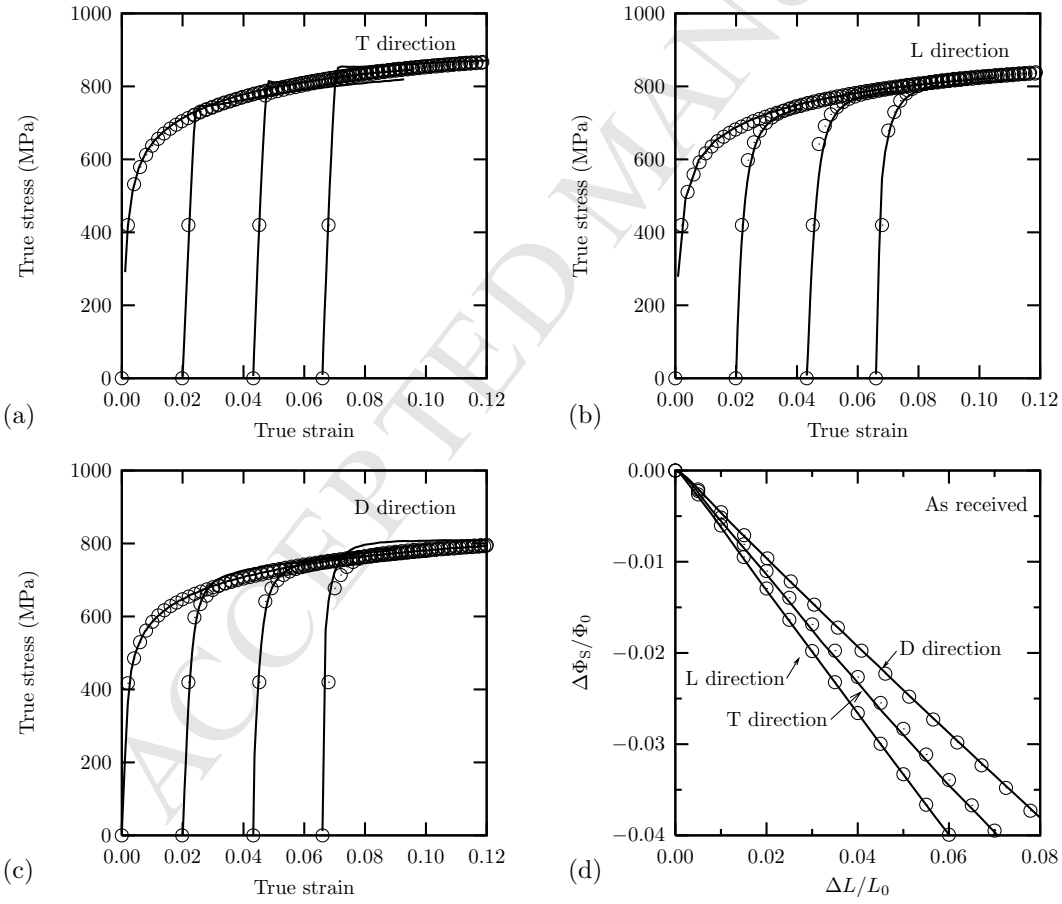


Fig. 9. Comparison of experimental (lines) and simulated (symbols) true stress-strain curves in smooth bar tests for T (a), L (b) and D (c) loading. (d) Diameter variation as a function of elongation for various loading directions (as received state).

Fig. 10 compares the experimental and simulated force-diameter reduction curves of NT specimens for both the as-received and prestrained materials. Because the developed model does not incorporate a damage model representing ductile failure, simulated and experimental curves are, here, compared up to ductile initiation point. For all types of notched bar specimens, the agreement is good up to the drop point for both load orientations and all prestrain levels. The results indicate that the developed model could be used for accurate prediction of stress triaxiality and equivalent strain at ductile fracture initiation which both are the most important factors (Decamp et al., 1997; Ohata and Toyoda, 2004) to develop a damage model representing ductility of anisotropic steels in the future.

Diameter reduction along the S direction as function of longitudinal strain of NT specimens loaded in T and L load directions is shown in Fig. 11 for the three notch geometries (as received state). The developed model can also represent anisotropic flow behavior in all NT specimens. Note that this set of data was not used for fitting material parameters.

Fig. 12 presents experimental and numerical stress-strain curves of tensile tests done in a plane strain state for as-received and 6% prestrained material. The simulations by the identified model accurately predict stress-strain responses in L direction (orthogonal to prestrain load) as well as in T direction (parallel to prestrain) for the as-received and the prestrained steels.

Fig. 13 shows the simulated yield surface for biaxial loading in the T–L plane after prestraining to the different experimentally prescribed levels (T direction). It is shown that hardening in initially strongly kinematic (as received $\rightarrow$ 2%) leading to a translation of the yield surface. Due to the high value of parameter $D$, $\underline{X}$ rapidly reaches its saturation value and hardening tends to become more isotropic (2%$\rightarrow$ 6%) with the yield surface growing.

## 6 Application to pipe bending simulation

The strain-based design methodology requires to carry out tests on large pipe elements (see e.g. (Timms et al., 2009; Tsuru and Agata, 2009)). The purpose of this section is to propose a finite element simulation of such tests taking into account the anisotropic material behaviour. Using the developed constitutive model, bending simulation of a pipe prestrained during the forming process was conducted to clarify the prestrain effect on the buckling capacity. In this study, prestraining was assumed to be monotonic plane strain tension along T direction and prestrain ($\varepsilon_{\mathrm{TT}}$) was applied up to 6 %. The zero strain direction corresponds to the L direction which is representative of UOE forming.

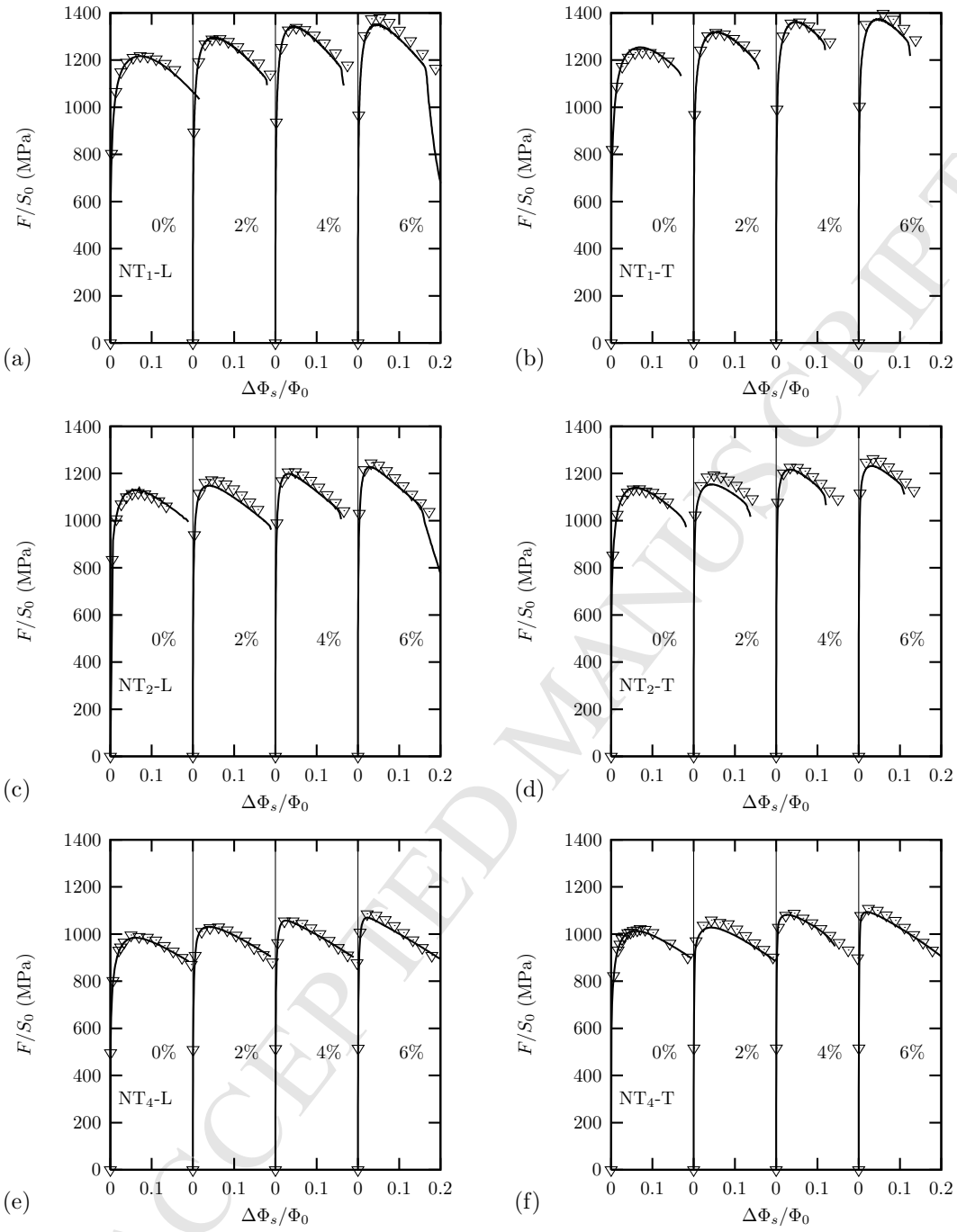


Fig. 10. Comparison of experimental (lines) and simulated (symbols) force-diameter reduction curves in notched bar tests

### *6.1 Finite element simulation of pipe bending experiments*

The finite element model for pipe is shown in Fig. 14. The nominal diameter ($D_n = 2R$) to the thickness ($t$) ratio of the pipe was 47. The length ($L$) was 8 times the

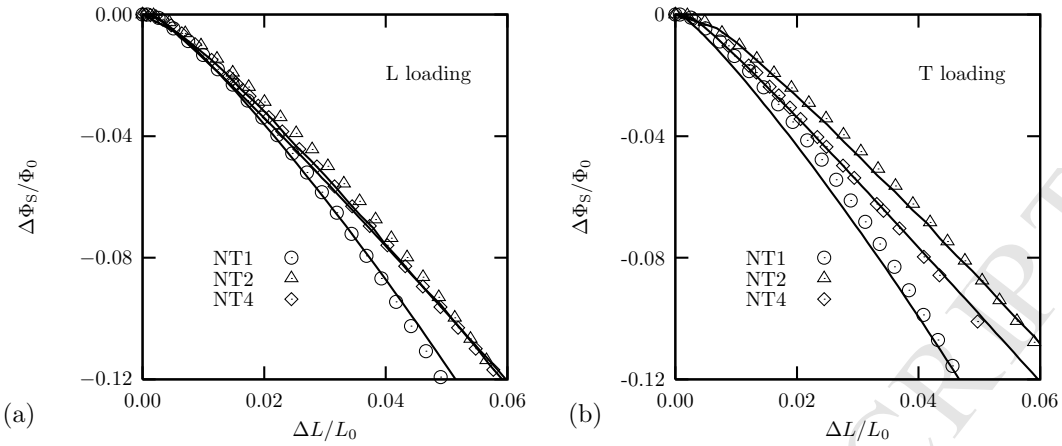


Fig. 11. Comparison of experimental (lines) and simulated (symbols) diameter reduction-longitudinal strain curves in notched bar tests (as received state).

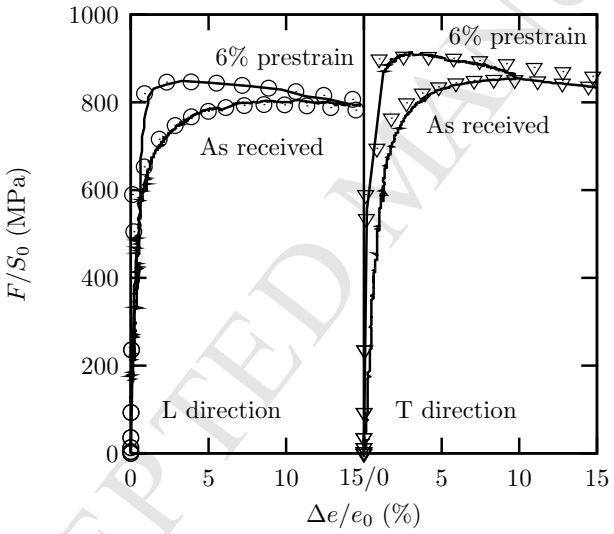


Fig. 12. Comparison of experimental (lines) and simulated (symbols) results of plain strain tests.

diameter. Due to symmetries, only $\frac{1}{4}$ of the the pipe was actually meshed. A local material frame is used to define the material principal directions (T, L and S) with respect to the pipe: L corresponds to the pipe axis and is constant whereas T and S vary depending on the angular position. All calculations were performed using 3D linear elements (eight nodes) using full integration and a F-bar formulation to avoid spurious pressure oscillations (Hughes, 1980). An initial internal pressure, $P$, equal to 80% of the burst pressure ($P_c$) is applied to tube. $P_c$ is given by:

$$P_c = \frac{2t}{D_n}\sigma_{\mathrm{X100}} \tag{11}$$

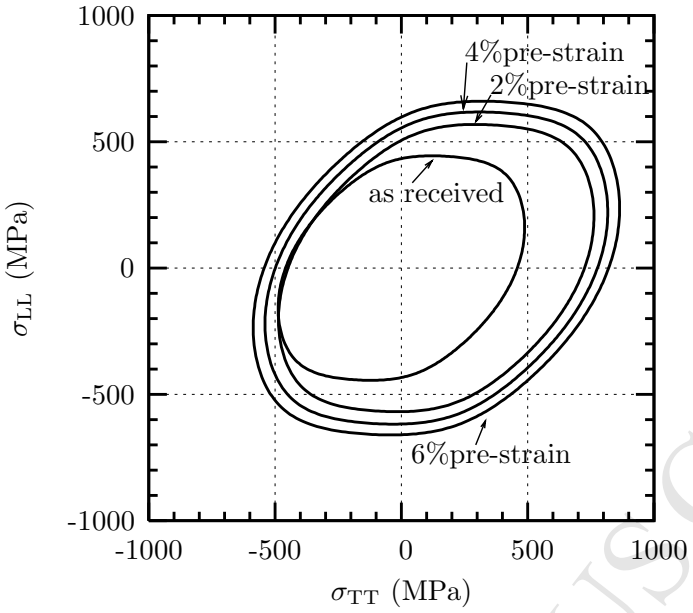


Fig. 13. The calculated yield loci of the used steel before and after prestraining.

where $\sigma_{\mathrm{X100}} = 100$ kpsi$= 690$ MPa (so that $P = 23.5$ MPa) . The bending angle ($\theta$) is then applied rotating a rigid plate attached on one pipe end. The rotation axis is allowed to move freely along the pipe axis to avoid generating spurious axial tensile forces. Simulations are carried out assuming either (i) pure bending or (ii) bending assuming an end-capped pipe so that an axial force equal to $\pi R^2 P$ is generated. In the following bending moments will be normalized by the pure bending limit load (Huh et al., 2007) assuming a flow stress equal to $\sigma_{\mathrm{X100}}$:

$$M_0 = D_n^2 t \sigma_{\mathrm{X100}} \tag{12}$$

In order to trigger buckling at the center of the pipe, a small geometric imperfection was inserted. It consists in a radial perturbation of the pipe diameter given following the shell theory proposed by Timoshenko (Tsuru et al., 2008). The perturbation is characterized by a wave length $\lambda$ equal to :

$$\lambda = 2\pi \left( \frac{D_n^2 t^2}{48(1-\nu^2)} \right)^{\frac{1}{4}} \tag{13}$$

so that $\lambda = 16.75t$ in the present case. The prescribed relative perturbation $\delta$ is expressed as: $\delta = (D_M - D_m)/D_n$ where $D_M$ and $D_m$ as respectively the maximum and minimum diameters (see fig. 14). The radial perturbation is expressed as:

$$\Delta R = \delta \frac{D_n}{4} \cos\left(2\pi \frac{z}{\lambda}\right) \quad \text{for} \quad |z| < \frac{3}{4}\lambda \quad \text{and} \quad 0 \quad \text{otherwise} \tag{14}$$

where $z$ denotes the longitudinal position (with $z = 0$ at the center of the pipe segment).

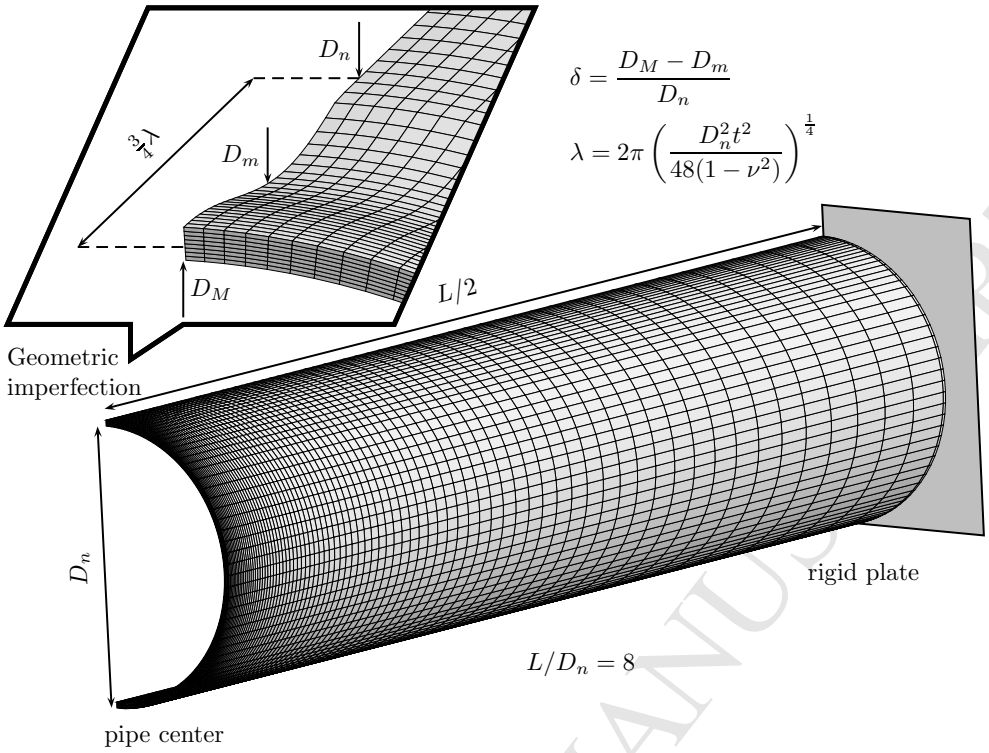


Fig. 14. FEA model of pipe bending and geometric imperfection ($\delta = 5\%$).

### *6.2 Simulation results*

Fig. 15 shows the effect of prestrain (between 0 and 6%) on bending behaviour under both pure bend and capped-end conditions. In both conditions, prestraining strongly affects the peak moment ($M_c$) and the angle at the onset of buckling ($\theta_c$), i.e. the angle corresponding to $M_c$. Both moment and angle are much higher under the end-capped condition than under pure bending. With increasing prestrain the peak moment increases while the critical angle decreases. In particular, the critical angle of a pipe bended under end–capped condition is strongly reduced by prestraining. A bulge is formed on the compressive side of the pipe (see fig. 15) for bending angles larger than $\theta_c$ is observed experimentally (see e.g. (Timms et al., 2009)). In long distance gas pipeline projects using the high design factor , the pipes buried under the ground might be subjected to move under end–capped condition. Furthermore, prestrain level due to pipe forming fluctuates along the circumferential direction of a line pipe. In the case of UOE pipes, the deviation of prestrain is distributed between $-20\%$ and $+50\%$ of the average prestrain level. Hence this numerical study suggests that prestrain history in pipe manufacturing process should be precisely controlled for line pipes used in strain-based design.

Fig. 16 shows the effect of defect size on the critical bending moment and on the critical bending angle for a prestrain level equal to 2%. The simulation of bending

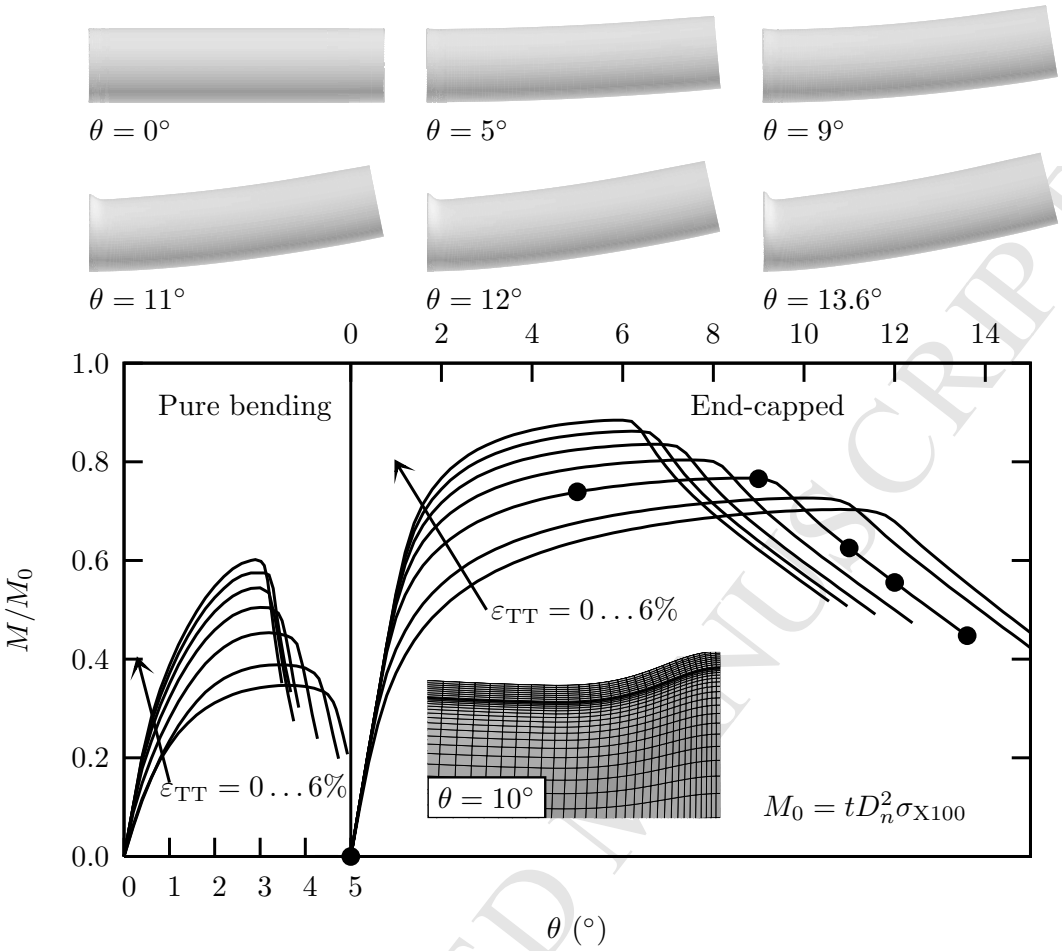


Fig. 15. Effect of prestrain on bending resistance. Deformed pipes correspond to the simulation assuming end-capped condition and a prestrain level of 2%. Symbols on the curve correspond to the various loading steps. A detail of the bulge formed during load drop is also shown for the same conditions at $\theta = 10°$.

was performed under two conditions: pure bending and end–capped. The critical buckling moment is not significantly affected by the pipe defect size. On the other hand, the defect size absolutely deteriorates the critical angle, especially under the end-capped condition. These results are similar to the previous study (Tsuru and Agata, 2009).

## 7 Conclusions

In this study, a phenomenological model has been developed for anisotropic materials with combined isotropic/kinematic hardening. The generic model was applied to describe the behaviour of a X100 grade line pipe steel. For this type

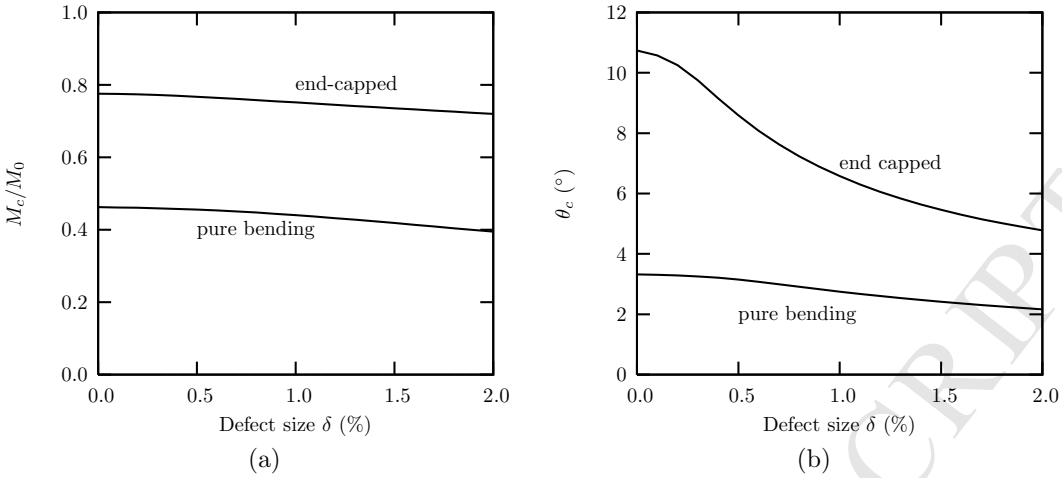


Fig. 16. Effect of geometric imperfection on strain capacity (2% prestrain).

of material, plastic anisotropy is caused by the specific crystallographic texture existing in the mother plate as well as by prestrain induced by cold forming. Incorporating kinematic hardening in the model is crucial to be able to represent prestrain induced anisotropy. The model was identified using tensile tests carried out on smooth and notched axisymmetric bars and plane strain specimens. In order to distinguish isotropic and kinematic hardening, these tests were carried out on as-received plate material as well as on prestrained materials. The model was implemented in a finite element code and used to perform simulations of large scale pipe bending experiments. The numerical results suggest that prestraining in the pipe forming process significantly affects the bending capacity of pipes.

*Acknowledgements*

The authors gratefully acknowledge financial support from Nippon Steel Corporation. The authors are deeply indebted to Dr. E. Tsuru (Nippon Steel Corporation) for valuable discussions about pipe bending simulation. Further, the authors wish to thank Mr. K. Nagai (Nippon Steel Corporation) for conducting prestrain tests.

## References

J.-H. Baek, Y.-P. Kim, C.M. Kim, W.S. Kim, and C.S. Seok, 2010. Effects of pre-strain on the mechanical properties of API 5L X65 pipe. Mater. Sci. Engng A 527 (6), 1473–1479.

F. Barlat, D.J. Lege, and J.C. Brem, 1991. A six–component yield function for anisotropic materials. Int. J. Plasticity 7, 693–712.

J. Besson and R. Foerch, 1997. Large scale object–oriented finite element code design. Comp. Meth. Appl. Mech. Engng 142, 165–187.

P.W. Bridgman, 1952. Studies in large plastic flow and fracture. McGraw–Hill.

F. Bron and J. Besson, 2004. A yield function for anisotropic materials. Application to aluminium alloys. Int. J. Plasticity 20, 937–963.

J.L. Chaboche, 1986. Time-independent constitutive theories for cyclic plasticity. Int. J. Plasticity 2, 149–188.

J.L. Chaboche, 2008. A review of some plasticity and viscoplasticity constitutive theories. Int. J. Plasticity 24, 1642–1693.

J.-L. Chaboche, 1989. Constitutive equations for cyclic plasticity and cyclic viscoplasticity. Int. J. Plasticity 5, 247–302.

K. Decamp, L. Bauvineau, J. Besson, and A. Pineau, 1997. Size and geometry effects on ductile rupture of notched bars in a C–Mn steel: Experiments and modelling. Int. J. Frac. 88 (1), 1–18.

L. Devillers-Guerville, J. Besson, and A. Pineau, 1997. Notch fracture toughness of a cast duplex stainless steel: modelling of experimental scatter and size effect. Nucl. Eng. Des. 168, 211–225.

D. P. Fairchild, W. Cheng, S. J. Ford, K. Minnaar, N. E. Biery, A. Kumar, and N. E. Nissley, 2008. Development of high-strength steel line pipe for SBD applications. Int. J. of offshore and polar engineering 18 (3), 220–225.

R. Foerch, J. Besson, G. Cailletaud, and P. Pilvin, 1997. Polymorphic constitutive equations in finite element codes. Comp. Meth. Appl. Mech. Engng 141, 355–372.

H. Haddadi, S. Bouvier, M. Banu, C. Maier, and C Teodosiu, 2006. Towards an accurate description of the anisotropic behaviour of sheet metals under large plastic deformations. Int. J. Plasticity 22, 2226–2271.

M. D. Herynk, S. Kyriakides, A. Onoufriou, and H. D. Yun, 2007. Effects of the UOE/UOC pipe manufacturing processes on pipe collapse pressure. Int. J. Mech. Sci. 49 (5), 533–553.

R. Hill, 1950. The mathematical theory of plasticity. Clarendon Press, Oxford.

T. Hoc and S. Forest, 2001. Polycrystal modelling of IF-Ti steel under complex loading path. Int. J. Plasticity 17, 65–85.

O.S. Hopperstad, M. Landseth, and S. Remseth, 1995a. Cyclic stress-strain behaviour of alloy AA6060, Part I: Uniaxial experiments and modelling. Int. J. Plasticity 11, 725–739.

O.S. Hopperstad, M. Landseth, and S. Remseth, 1995b. Cyclic stress-strain behaviour of alloy AA6060 T4, Part II: Biaxial experiments and modelling. Int. J. Plasticity 11, 741–762.

T.J.R. Hughes, 1980. Generalization of selective integration procedures to anisotropic and non linear media. Int. J. Numer. Meth. Engng 15, 1413–1418.

N.S. Huh, Y.J. Kim, and Y.J. Kim, 2007. Limit load solutions for pipes with through-wall crack under single and combined loading based on finite element analyses. J. Pressure Vessel Technol. 129, 468–472.

A.P. Karafillis and M.C. Boyce, 1993. A general anisotropic yield criterion using bounds and a transformation weighting tensor. J. Mech. Phys. Solids 41, 1859–1886.

D. Kim, F. Barlat, S. Bouvier, M. Rabahallah, T. Balan, and K. Chung, 2007. Non-quadratic anisotropic potentials based on linear transformation of plastic strain rate. Int. J. Plasticity 2, 1380–1399.

D.H. Lee, B.H. Kim, H. Lee, and J.S. Kong, 2009. Seismic behavior of a buried gas pipeline under earthquake excitations. Eng. Struct. 31 (5), 1011–1023.

R.W. Logan and W.F Hosford, 1980. Upper-bound anisotropic yield locus calculations assuming (111)-pencil glide. Int. J. Mech. Sci. 22 (7), 419–430.

A.C. Mackenzie, J.W. Hancock, and D.K. Brown, 1977. On the influence of state of stress on ductile failure initiation in high strength steels. Eng. Fract. Mech. 9, 167–188.

H. Mecking and U.F. kocks, 1981. Kinetics of flow and strain-hardening. Acta Metall. 29 (11), 1865–1875.

G. Mirone, 2004. A new model for the elastoplastic characterization and the stressstrain determination on the necking section of a tensile specimen. Int. J. Solids Structures 2004, 3545–3564.

M Ohata and M Toyoda, 2004. Damage concept for evaluating ductile cracking of steel structure subjected to large-scale cyclic straining. Sci. Technol. Adv. Mater. 5 (1-2), 241–249.

F. Rivalin, J. Besson, M. Di Fant, and A. Pineau, 2000. Ductile tearing of pipeline-steel wide plates — II.: Modeling of in–plane crack propagation. Eng. Fract. Mech. 68 (3), 347–364.

K. Sai, G. Cailletaud, and S. Forest, 2006. Micro-mechanical modeling of the inelastic behavior of directionally solidified materials. Int. J. Plasticity 38, 203–217.

H. Samrout, R. ElAbdi, and J.L. Chaboche, 1997. Model for 28CrMoV5-8 steel undergoing thermomechanical cyclic loadings. Int. J. Solids Structures 34 (35-36), 4547–4556.

Y. Shinohara, E. Tsuru, H. Asahi, T. Hara, Y. Terada, N. Doi, N. Ayukawa, and M. Murata, 2008. Development of high-strength steel line pipe for SBD applications. Int. J. of offshore and polar engineering 18 (3), 220–225.

F. Sidoroff and A. Dogui, 2001. Some issues about anisotropic elastic-plastic models at finite strain. Int. J. Solids Structures 38, 9569–9578.

J.C. Simo and R.L. Taylor, 1985. Consistent tangent operators for rate–independent elastoplasticity. Comp. Meth. Appl. Mech. Engng 48, 101–118.

B. Tanguy, T.T. Luu, G. Perrin, A. Pineau, and J. Besson, 2008. Plastic and damage behavior of a high strength X100 pipeline steel: experiments and modelling. Int. J. of Pressure Vessels and Piping 85 (5), 322–335.

V. Tarigopula, O. S. Hopperstad, M. Langseth, and A. H. Clausen, 2008. Elastic-plastic behaviour of dual phase, high-strength steel under strain-path changes. Eur. J. Mech./A 27A, 764–782.

V. Tarigopula, O. S. Hopperstad, M. Langseth, and A. H. Clausen, 2009. An evaluation of a combined isotropic-kinematic hardening model for representation of complex strain-path changes in dual-phase steel. Eur. J. Mech. A-Solids 28 (4), 792–805.

C. Teodosiu and Z. Hu, 1995. Evalution of the intragranular microstructure at moderate and large strains. In: Proceedings of the 5th NUMIFORM conference. Simulation of materials proceeding: Theoroy, Methods and Applications.

C.M.J. Timms, D.D. DeGeer, M.R. Tsuru Chebaro, and E. Tsuru, 2009. Compressive strain limits of large diameter X80 UOE linepipe. In: Proc. 19th international offshore and polar engineering (ISOPE) conference, Osaka 21-26 june 2009.

E. Tsuru and J. Agata, 2009. Buckling resistance of line pipes with girth weld evaluated by new computational simulation and experimental technology for full-scale pipes. In: Proc. 19th international offshore and polar engineering (ISOPE) conference, Osaka 21-26 june 2009.

E. Tsuru, Y. Shinohara, and H. Asahi, 2008. Evaluation precept for buckling resistance of high-strength uoe line pipes used in strainbased design SBD applications. Int. J. of offshore and polar engineering 18 (3), 176–182.

Y. Wang and M. Liu, 2007. The role of anisotropy, toughness transferability and weld misalignment in the strain based design of pipelines. In: Proc. 17th international offshore and polar engineering (ISOPE) conference, Lisbon 1-6 july 2007.

Z.L. Zhang, M. Hauge, J. Ødegård, and C. Thaulow, 1999. Determining material true stress–strain curve from tensile specimens with rectangular cross–section. Int. J. Solids Structures 36, 3497–3516.

N. Zouhal, A. Molinari, and L.S. Tóth, 1996. Elastic-plastic effects during cyclic loading as predicted by the Taylor–Lin model of polycrystal elasti-viscoplasticity. Int. J. Plasticity 12 (3), 343360.

**List of Figures**

**List of Tables**